29th AIAA Applied Aerodynamics Conference
27 - 30 June 2011, Honolulu, Hawaii

AIAA 2011-3659

Stability Characteristics of Micro Air Vehicles from Experimental Measurements

Daniel V. Uhlig* and Michael S. Selig†

University of Illinois at Urbana-Champaign, Urbana, IL 61801, USA

A motion tracking system was used to experimentally determine the aerodynamic forces and moments of two micro UAVs. The airplanes have wingspans ranging from approximately 9 to 15 in and fly at Reynolds numbers below 25,000. The motion track provided a time history of the position and attitude and was used to derive the aerodynamic moments and analyze the stability derivatives of the airplanes. A reconfigurable hand-launched glider was used to show results for different wing configurations. In addition to the glider, a small commercially manufactured SU-26xp airplane was used. The longitudinal stability measurements from experimental data showed both airplanes to be more stable than predictions based on geometry. The SU-26xp airplane was used to study the effects of elevator deflection on trim flight conditions. In addition, the lateral stability terms for both airplane were measured. By understanding the stability and control over a range of flight conditions, a better understanding of the control of micro UAVs can be developed.

Nomenclature

a_x, a_y, a_z	=	body-axis translational acceleration
$\mathcal{AR}$	=	aspect ratio
b	=	wingspan
c	=	wing chord
S	=	wing or tail area
C_D	=	drag coefficient
C_{D_o}	=	parasite drag coefficient
C_L	=	lift coefficient
C_{L_α}	=	lift curve slope
C_l, C_M, C_N	=	roll, pitch, and yaw coefficients
D	=	drag
$\mathbf{F}$	=	force
I_{xx}, I_{yy}, ...	=	mass moments of inertia
L	=	lift
l_{ac}	=	distance from reference point to aerodynamic center
m	=	airplane mass
p, q, r	=	roll, pitch and yaw rates
$\mathbf{R}$	=	transformation or rotation matrix
SM	=	static margin
u, v, w	=	body-fixed translational velocity
V	=	inertial speed
α	=	angle of attack
β	=	sideslip angle
δ_e	=	elevator deflections (trailing edge down is positive)

*Graduate Student, Department of Aerospace Engineering, 104 S. Wright St., AIAA Student Member.
†Associate Professor, Department of Aerospace Engineering, 104 S. Wright St., Senior Member AIAA.
http://www.ae.illinois.edu/m-selig

$\partial\epsilon/\partial\alpha$	=	downwash from main wing at the tail
ϕ, θ, ψ	=	roll, pitch and heading angles
η_t	=	velocity deficit at tail
ω	=	angular rate

Subscripts

ac	=	aircraft
b	=	body-fixed frame
E	=	Earth-fixed axis system
G	=	due to gravity
t	=	horizontal tail
w	=	wing
x, y, z	=	body-fixed axis system directions
α, β	=	derivative per angle of attack or sideslip angle

I. Introduction

Very small airplanes with wingspans less than 50 cm (20 in) and weighing less than 100 g (3.5 oz) are starting to become readily available, and smaller micro Unmaned Aerial Vehicles (UAVs) are becoming more capable. The aerodynamics of very small aircraft are different from the better understood problem of larger UAVs. First, micro UAVs fly at significantly lower Reynolds number which introduces nonlinearities in the aerodynamic characteristics. Secondly, due to structural efficiencies, the ratio between inertial, gravitational and aerodynamic forces is different from those of larger aircraft, and this difference changes the dynamic response in flight. Finally, small aircraft often fly over a larger range of angles of attack to increase maneuverability to operate within confined spaces. In order to better understand the aerodynamics of micro UAVs, actual flight measurements are needed. The lift and drag results for a small airplane at extreme angles of attack was previously presented and forms the basis of this expanded work into stability and control characteristics of two small airplanes.[1]

A study at the University of Minnesota of a micro UAV in free-flight used a small 2-g (0.07-oz) glider to investigate micro-scale aerodynamics. The small glider was hand launched and not controlled.[2,3] From the flight trajectory, basic aerodynamic properties such as C_L, C_D, and C_M were calculated over a range of angles of attack. Rhineheart[2] calculated stability derivatives for the small free-flight glider. Mettler[3] continued the work by showing a single flight of the glider pitching up until it stalled and then pitching down rapidly.

Wind tunnel studies show that the aerodynamic properties of airfoils and wings change at low Reynolds numbers.[4–11] The studies looked at the lift and drag for airfoils and different aspect ratio wings and showed drag increasing and the lift curve slope decreasing with lower Reynolds numbers. Most studies did not include moment data, but one study at low Reynolds numbers by Mueller[12] showed the quarter chord moment was not constant with angle of attack.

To gather in-flight data from aircraft, traditionally, on-board sensors have been used.[13–15] However, due to size and weight constraints, micro UAVs have required off-board measurement. The most widely used off-board measurement approach has been a set of cameras that can track objects based on triangulation. A multiple infrared camera system built by Vicon Motion Systems Limited has been widely used in the motion capture field and has also been used by robotics researchers.[16] Many micro-scale UAV researchers have used the Vicon system to provide accurate positioning data for aerodynamic analysis.[2,3,17,18]

The Vicon camera system has been used to track and control small and micro UAVs, and the system has been used to test control laws for many different small aircraft because it offers flexibility of quickly attaching lightweight markers that are used for tracking. Vicon systems have been used to pursue many controls problems including implementing new controllers and researching multi-agent control using fleets of small-scale helicopters.[15,19–24]

For this research, a Vicon motion capture system with eight infrared cameras was used.[16] Using infrared lights, the cameras tracked reflective markers placed on the airplanes. By combining sets of markers to form an object, the system can track the position as well as the orientation of the aircraft as it flies in the

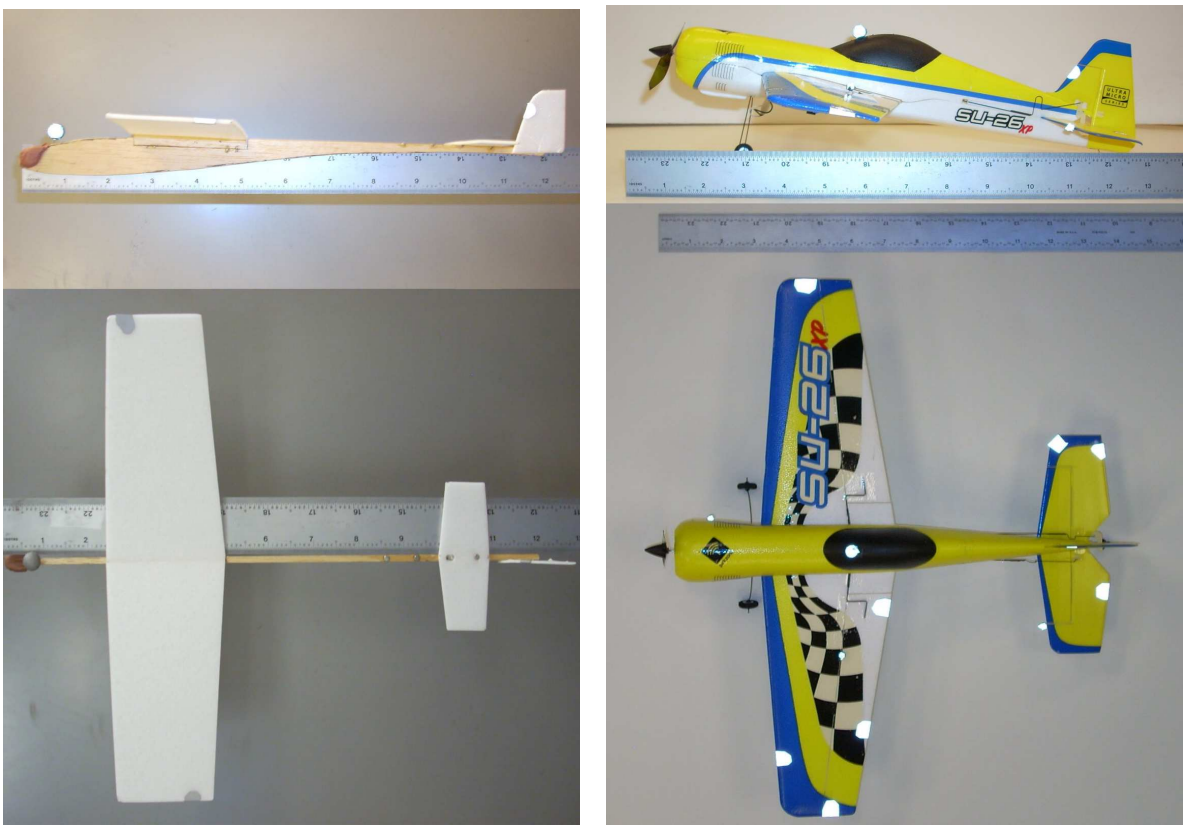

(a) Hand-launched free-flight glider

(b) SU-26xp RC airplane

Figure 1. Side and topview of the two airplanes used in the experiments with the attached reflective markers.

test environment. The Vicon software returns both position and orientation of the airplane in the Earth-referenced frame, and these data are analyzed to obtain the velocities and accelerations in the body-fixed frame.

A multiple-camera Vicon system is capable of accurate measurements as analyzed by Mettler, but the measurements still have noise.[3] In order to minimize the noise, a variety of filtering techniques were used.[13] By using techniques to reduce the noise and generate accurate position data, reliable results were obtained. The resulting data set included enough information that system identification approaches could be used to calculate aerodynamic parameters.[13,14]

In this research, a re-configurable free-flight glider and a larger RC airplane with control surfaces were used to gather flight test data using an eight-camera Vicon system in an indoor environment. Using the aircraft position time history, estimates of the aerodynamic characteristics of the aircraft were developed.

II. Experimental Apparatus

For this experiment, a 6.0-g (0.21-oz) hand-launched glider was constructed from balsa wood and Depron foam with a tapered wing and horizontal tail as shown in Fig. 1(a). The interchangable wing and horizontal tail were attached with tiny magnets so that the lifting surfaces could easily be switched and the horizontal tail could be moved fore or aft. By varying the incidence angle, wing aspect ratio, and the airplane center of gravity, the glider was tested in a variety of configurations.

In addition to the glider, a commercially manufactured, 40.0-cm (15.75-in) wingspan, 36.6-g (1.29-oz) RC scale SU-26xp airplane shown in Fig. 1(b) was used.[25] It was built from precisely formed styrofoam, and the wing was a symmetric airfoil with 11% thickness. A small battery powered a RC receiver controlled three servos and the speed control for the miniature electric motor. The airplane had actuated control surfaces that included ailerons, elevator and rudder. The tail surfaces were flat plates with minimal thickness.

Table 1. Physical Properties of the Hand-Launched Glider

Property	Metric Measurement	Units	English Measurement	Units
m	8.45	g	5.79×10^{-4}	slugs
I_{xx}	8.11×10^{-6}	kg-m^2	5.98×10^{-6}	slugs-ft^2
I_{yy}	4.54×10^{-5}	kg-m^2	3.35×10^{-5}	slugs-ft^2
I_{zz}	5.28×10^{-5}	kg-m^2	3.90×10^{-5}	slugs-ft^2
I_{xz}	1.87×10^{-6}	kg-m^2	1.38×10^{-6}	slugs-ft^2
I_{yz}	8.05×10^{-8}	kg-m^2	5.94×10^{-8}	slugs-ft^2
I_{xy}	-1.78×10^{-8}	kg-m^2	-1.31×10^{-8}	slugs-ft^2
Small Wing				
Wingspan	24.4	cm	9.6	in
Wing area	144.0	cm^2	22.32	in^2
Wing chord (at root)	6.6	cm	2.6	in
Wing chord (at tip)	5.21	cm	2.05	in
Wing thickness	0.178	cm	0.07	in
Wing dihedral	4.5	deg		
Large Wing				
Wingspan	30.4	cm	11.98	in
Wing area	177.7	cm^2	27.55	in^2
Wing chord (at root)	6.6	cm	2.6	in
Wing chord (at tip)	5.08	cm	2.0	in
Wing thickness	0.178	cm	0.07	in
Wing dihedral	4.5	deg		
Airplane length	31.75	cm	12.5	in
Horizontal tail area	19.35	cm^2	3.0	in^2
Vertical tail area	9.44	cm^2	1.46	in^2

The geometric and mass properties for the hand-launched glider are listed in Table 1, and SU-26xp airplane properties are listed in Table 2. The moments of inertia were calculated by subdividing the airplanes into small sections that were then weighed individually. By combining the moments of inertia and the position of the numerous small pieces, the overall moments of inertia were calculated. The total mass and location of the center of gravity was calculated the same way.

Eight infrared cameras, each with its own infrared light source, were used by the Vicon system to track circular reflections. Small reflective markers were attached to the airplanes to generate strong reflections and are shown by the white or silver spots in Fig. 1. Using multiple camera views, the Vicon software triangulated the reflections in three dimensions. The resulting position and attitude track was recorded at a rate of 200–300 Hz.

Each airplane was modeled in the Vicon software by tracking multiple objects so different parts could be tracked separately during the flights. For each object, the Earth-referenced position and the Euler angles were recorded. First, the fuselage and wing were combined as a single object to provide the basic airplane position and attitude information throughout the flight. Small markers (approximately 0.2-in diameter) were positioned toward each of the wingtips as well as the along the fuselage. Second, the control surfaces had sets of small markers attached so that the attitude relative to the fuselage could be calculated. Tracking data for each of the objects was recorded and later post processed to provide useful information on the airplane aerodynamic performance.

Free-flight unpowered glides were used to gather data without any thrust. The flights included steady glides as well as shallow stalls and stall recoveries. The launch speed and angle as well as the center of gravity and control surface positions were adjusted to vary the flight trajectory of the airplane. The gliding

Table 2. Physical Properties of the SU-26xp Test Airplane

Property	Metric Measurement	Units	English Measurement	Units
m	36.04	g	2.47×10^{-3}	slugs
I_{xx}	1.26×10^{-4}	kg-m^2	9.31×10^{-5}	slugs-ft^2
I_{yy}	2.31×10^{-4}	kg-m^2	1.70×10^{-4}	slugs-ft^2
I_{zz}	3.44×10^{-4}	kg-m^2	2.53×10^{-4}	slugs-ft^2
I_{xz}	-2.17×10^{-6}	kg-m^2	-1.66×10^{-6}	slugs-ft^2
I_{yz}	5.50×10^{-7}	kg-m^2	4.05×10^{-7}	slugs-ft^2
I_{xy}	-3.58×10^{-6}	kg-m^2	-2.64×10^{-6}	slugs-ft^2
Wingspan	40.05	cm	15.75	in
Wing area	312.45	cm^2	48.4	in^2
Wing chord (at root)	10.16	cm	4.0	in
Wing chord (at tip)	5.46	cm	2.15	in
Wing thickness	11.0%			
Wing incidence angle	0.0	deg		
Wing dihedral	0.0	deg		
Airplane length	34.93	cm	13.75	in
Horizontal tail area	79.87	cm^2	12.38	in^2
Elevator area	51.48	cm^2	7.98	in^2
Vertical tail area	45.24	cm^2	7.01	in^2

flights were constrained by the environment dimensions to 1–2 sec of useful data. Gliding flights were used because the only forces acting on the airplane were from gravity and aerodynamic loads; the thrust force from the propeller was not present and did not need to be estimated. The aerodynamic loads were the only unknowns. By combining these different tests, a detailed model of the airplane aerodynamic performance was developed using system identification techniques described in Section III. Multiple flights of each type were used to generate a rich set of data.

III. Data Acquisition and Post Processing

The data stream provided by the Vicon system included the Earth-referenced position and the Euler angles for each of the four objects. The tracking system provided information on whether the object, that is a control surface or fuselage, was visible to the camera system and if it was, the attitude and position of the object. The tracking data from each object was filtered to acquire useful measurements.

For the fuselage object, the position and attitude were used in the post processing. The attitude, angular rates, velocities and accelerations were required to analyze the airplane performance. The first step was to transform the raw measured data from object-fixed reference frame as recorded by the tracking system to the center of gravity of the airplane. By measuring the distance and rotation between the airplane center of gravity and the object-fixed origin, the rotation and offset between the object measured frame and the airplane center of gravity body-fixed frame were known. In order to combine the measured offsets and the Earth-referenced tracking data, transformation matrices were used. Each transformation matrix includes a set of angular offsets (θ_o, ϕ_o, ψ_o) and a set of position offsets (x_o, y_o, z_o) as shown below:

$$\mathbf{R} = \begin{bmatrix} \cos\theta_o \cos\psi_o & \cos\theta_o \sin\psi_o & -\sin\theta_o & x_o \\ \sin\phi_o \sin\theta_o \cos\psi_o - \cos\phi_o \sin\psi_o & \sin\phi_o \sin\theta_o \sin\psi_o - \cos\phi_o \cos\psi_o & \sin\phi_o \cos\theta_o & y_o \\ \cos\phi_o \sin\theta_o \cos\psi_o - \sin\phi_o \sin\psi_o & \cos\phi_o \sin\theta_o \sin\psi_o - \sin\phi_o \cos\psi_o & \cos\phi_o \cos\theta_o & z_o \\ 0 & 0 & 0 & 1 \end{bmatrix} \quad (1)$$

A matrix was first developed for the transformation from the airplane object measurement frame to the

airplane center of gravity body-fixed frame. The resulting matrix was labeled $\mathbf{R}_{measured\ to\ CG}$. The second transformation matrix, $\mathbf{R}_{inertial\ frame}$, was from the Earth-fixed inertial reference frame to the tracking object center and was recorded at each time step. By combining these two rotations through the multiplication of $\mathbf{R}_{measured\ to\ CG}$ and $\mathbf{R}_{inertial\ frame}$, the transformation from the Earth-fixed reference frame to the airplane center of gravity was calculated.

$$\mathbf{R}_{ac} = \mathbf{R}_{measured\ to\ CG} \cdot \mathbf{R}_{inertial\ frame} \tag{2}$$

From the resulting $\mathbf{R}_{ac}$ matrix, the Earth-referenced attitude and position at the airplane center of gravity were determined by calculating θ, ϕ, and ψ as well as x, y, and z.

The second step was to find any timesteps in the data where the system had lost track of the object, which were usually only a few consecutive measurements during a flight. Out of the total flight time of 1-2 sec, typically no more than 0.005–0.025 sec of data were missing. In these regions, a linear fit was used between the measurements at either side of the missing data. After filling in these few points, the noise in the raw measurements was smoothed using the Matlab implementation of the robust local regression with a second-order polynomial (the *smooth* function with the *'rloess'* option).[26] In order to limit the effect of any measured points that were significantly off the general trend line, the robust method was chosen. To find the velocity and acceleration, the smoothed data was differentiated using a fourth-order local fitting method developed by Klein and Morelli.[13] For both the position and attitude, the same filtering techniques were used to estimate the airplane track.

From the smoothed and differentiated data, the position of the airplane along with the velocity and acceleration in the Earth-referenced frame as well as the Euler angles were known. To transform these quantities into a body-fixed reference frame, a rotation matrix [see Eq. (1)] based on the Euler angles was used.[3,27] First, the velocity and acceleration were transformed to the body-fixed frame using

$$\mathbf{V}_b = [\ u\ v\ w\ ]^T \quad = \mathbf{R}_{earth\ to\ body}\ \ [\ \dot{x}_E\ \dot{y}_E\ \dot{z}_E\ ]^T \tag{3a}$$

$$\mathbf{a}_b = [\ a_x\ a_y\ a_z\ ]^T = \mathbf{R}_{earth\ to\ body}\ \ [\ \ddot{x}_E\ \ddot{y}_E\ \ddot{z}_E\ ]^T \tag{3b}$$

By applying the transformations, the body-fixed axis velocity and acceleration were known. The Euler rates were calculated by transforming the Euler angular rates to the body-fixed angular rates.[3,13]

$$\begin{bmatrix} p \\ q \\ r \end{bmatrix} = \begin{bmatrix} 1 & 0 & -\sin\theta \\ 0 & \cos\phi & \sin\phi\cos\theta \\ 0 & -\sin\phi & \cos\phi\cos(\theta) \end{bmatrix} \begin{bmatrix} \dot{\phi} \\ \dot{\theta} \\ \dot{\psi} \end{bmatrix} \tag{4}$$

With all of these quantities known over the duration the flight, the analysis of the aerodynamic performance could be completed. To obtain the angle of attack and sideslip angle, the measured inertial speeds can be used if two assumptions were made. First, the air was assumed to be perfectly still, and second the induced flow affects on the airplane were ignored. With these assumptions, a good estimate of the freestream flow angles was made using

$$\alpha = \arctan(w/u) \tag{5a}$$

$$\beta = \arcsin(v/V) \tag{5b}$$

The true values of α and β remain unknown, but a good estimate of the angles were made using the inertial speeds in Eq. 5(a-b).

The forces acting on the airplane were known since the mass of the airplane was fixed, and the body-fixed axis accelerations (a_x, a_y, a_z) were known from the position tracking data. The total external forces acting on the airplane were calculated using

$$\mathbf{F}_{external} = [\ a_x\ a_y\ a_z\ ]^T\ m \tag{6}$$

By subtracting the force of gravity ($\mathbf{F}_G$) from the total external forces, the aerodynamic forces acting on the airplane were determined.

$$\mathbf{F}_{aero} = \mathbf{F}_{external} - \mathbf{F}_G \tag{7}$$

Table 3. The Parameters Defining the Airplane State in the Experiments

Acceleration	a_x, a_y, a_z
Airspeed	V
Angle of attack	α
Control surface deflection	δ_e, δ_r, δ_a
Drag force	D
Dynamic pressure	q
Lift force	L
Moments	M_x, M_y, M_z
Pitch, roll and yaw angles	θ, ϕ, ψ
Pitch, roll and yaw rates	p, q, r
Sideslip angle	β
Time	t
Velocity	u, v, w

Three resulting components of $\mathbf{F}_{aero}$ were in the body-fixed axis frame and were due to aerodynamic loading on the airplane. To calculate lift and drag, which are the force components in the wind axis, the forces in the body frame needed to be transformed into the wind frame using

$$L = -F_z \cos\alpha + F_x \sin\alpha \tag{8a}$$

$$D = -F_z \sin\alpha \cos\beta - F_x \cos\beta \cos\alpha - F_y \sin\beta \tag{8b}$$

By not making a small angle approximation on the sideslip angle, β, in the drag calculations, the result was more accurate for a maneuvering airplane. The angle of attack and sideslip angle were calculated throughout the flight to understand the performance of the airplane.

To calculate the moments being generated by the aerodynamic loads on the airplane, a similar method to the approach used to calculate the forces was implemented. Starting with the body-fixed angular rates (p, q, r) and the moments of inertia, the moments acting on the airplane were found using the rotational equation of motion[3,13] that is

$$\frac{d^2(\mathbf{I}\,\omega)}{dt^2} = \mathbf{M}_{aero} \tag{9}$$

The airplane moments of inertia shown in Table 2 were used, and the standard assumption to ignore I_{xy} and I_{yz} was applied. Those two terms could be ignored because the airplane is almost symmetric about these axes, and the values are very small. The moments acting on the airplane were calculated with respect to the airplane center of gravity.

$$[M_x\ M_y\ M_z]^T = \mathbf{I}_b[\dot{p}\ \dot{q}\ \dot{r}\ ]^T + [p\ q\ r]^T \times \mathbf{I}_b[p\ q\ r]^T \tag{10}$$

These three equations represent the roll, pitch, and yaw moments being generated by the aerodynamic forces about the center of gravity. The moments are important to understanding the response of the airplane, particularly the response to control surface deflections.

By processing all of the data, a complete time history of the airplane state was recorded. The aerodynamic forces and moments were found via the aforementioned approach and the aerodynamic properties of the airplane could be analyzed. In order to perform a thorough analysis, additional variables such as atmospheric density and mass properties were measured and used in the analysis. A list of all of the recorded and calculated variables is shown in Table 3.

IV. Results and Discussion

A. Lift and Drag Performance

The lift and drag results are presented for the glider in Fig. 2 and for the SU-26xp in Fig. 3. In each case, the data points of the complete time history are plotted along with the subset of data points with low angular

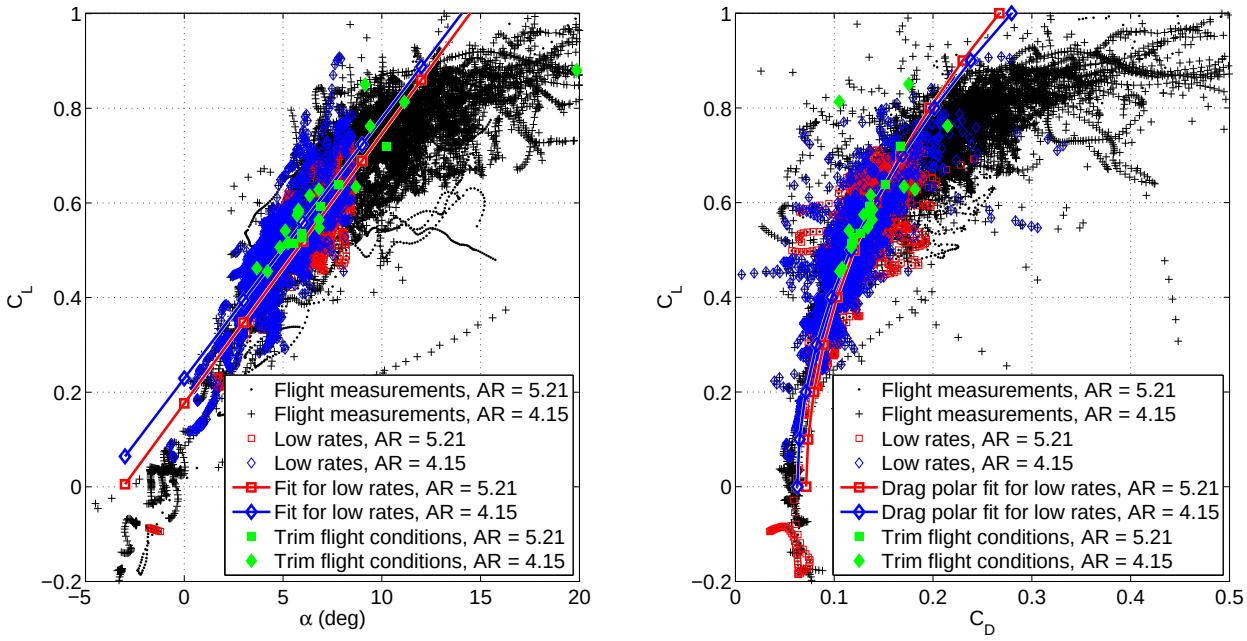

Figure 2. Experimentally measured lift and drag coefficients for two different aspect ratio wings on the glider.

rates (LAR) which had limits on angular rates ($\dot{\alpha} < 20$ deg/sec; $\dot{\beta}$, p, q, $r < 60$ deg/sec). The flights were to some degree unsteady so unsteady flight dynamics effects were a factor in the data. By limiting the angular rates, however, the dynamic effects could be minimized. To find the lift curve slope for each airplane, a linear least squares fit was found using the LAR data. The LAR data was selected instead of the complete data set to minimize the dynamic effects. Finally, to show the trim conditions, the pitching moment results from each flight were used to find the trim angle for that flight. The flights were then combined over a small range of trim angle of attack (0.75 deg), and the combined data set was used to find a $C_{L_{\text{trim}}}$ and $C_{D_{\text{trim}}}$ value for the trim angle of attack of each data set.

Figure 2 co-plots the lift and drag results for glider with a wing aspect ratio of 5.21 and 4.15. The complete data set is shown along with a subset used for least squares fit which used $\alpha < 8.5$ deg to avoid the nonlinear effects of stall. For each configuration, a least squares fit shows the experimental lift curve slope of the glider. In each case, the zero lift angle was different due to variations in incidence angle between the two wings. The linear lift curve slope, C_{L_α}, was 3.26/rad and 3.14/rad for the larger and smaller aspect ratio wings, respectively.

To compare to theory and other results in the literature, Prandtl lifting line theory was used to find theoretical results for the two different aspect ratios. In order to correct for low Reynolds number effects, the theoretical lift curve slope should be decreased by a factor (K_{Re})

$$C_{L_\alpha} = K_{Re}\frac{2\pi(\mathcal{AR})}{(\mathcal{AR}+2)} \tag{11}$$

Spedding[11] tested a E387 airfoil and wing at low Reynolds number of 10,000–60,000 and found that with decreasing Reynolds numbers the lift curve slopes also decreased. At a Reynolds number of 15,000 a correction factor of approximately 0.71 was required. The glider flew at a Reynolds number of 14,100 and 15,600 for the large and small wing respectively. The larger wing had more wing area and flew at a lower speed and hence a lower Reynolds number (the chord of each of the wings was the same). From the experimental results, K_{Re} was found to be 0.72 and 0.74 for the glider with the large and small wing, respectively.

Similarly, for the SU-26xp airplane the whole data set is shown in Fig. 3 along with the low angular rate data and the trim flight points. The lift curve slope of the airplane was found to be 3.61/rad based on a least squares fit of the low angular rate data below an angle of attack of 9 deg. Using Prandtl lifting line theory and the aspect ratio of 5.12, the lift curve slope should be 4.52/rad. From the experimental results, the low

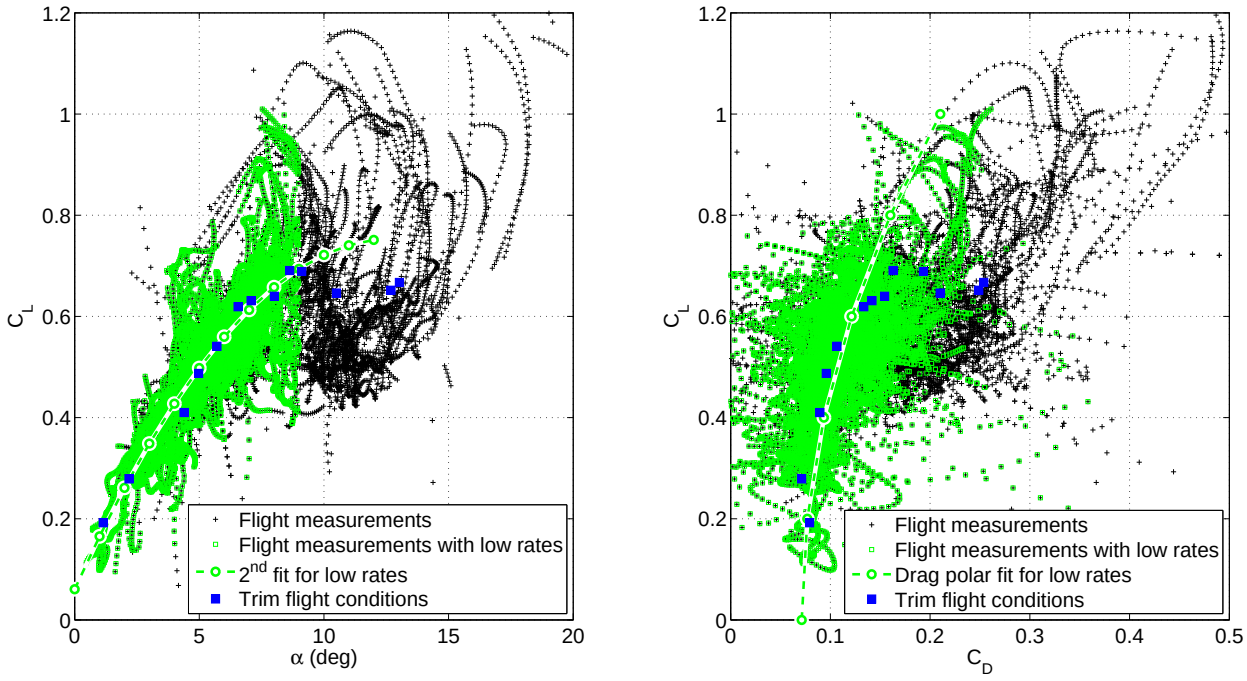

Figure 3. Experimentally measured lift and drag coefficients of the SU-26xp.

Reynolds number correction factor was found to be 0.80 for the SU-26xp which is close to the estimate from Spedding[11] of 0.76 at a Reynolds number of 22,300. The correction factor value is slightly larger than for the glider, which means that the higher Reynolds number wing has a higher lift curve slope. While still less than the linear lifting line prediction, the increase in lift curve slope is expected since the SU-26xp has a higher Reynolds number relative to the glider (22,300 versus approximately 15,000 for the glider). A second-order fit is used to show that the lift curve decrease gradually before $C_{L_{\max}}$. The decrease in lift curve slope is probably due to laminar separation.

The drag polar for the glider (see Fig. 2) shows the induced drag increasing faster with the smaller aspect ratio wing as expected. The smaller wing has a C_{D_o} that is less than the larger wing due to the small increase in Reynolds number and as well as differences in the interference drag between the two wings. The larger wing flies at a Reynolds number of 14,100 which is lower than the Reynolds number of the small wing (15,600) which accounts for some of the change in C_{D_o}. While both wings have approximately the same chord, the larger wing flies at a slower speed since it has a greater wing area. In addition, the minimum drag depends on how specific parts of the airplane interact with the flow. Parts such as the reflective markers, nose weights, and the wing attachment vary between the two configurations of the glider and account for a significant portion of the interference and form drag.

For the SU-26xp, the experimental drag polar plot in Fig. 3 was used to fit a drag polar. The second-order drag polar fit over the low angular rate data fits the effect of the induced drag well until separation occurs at $C_L \approx 0.7$ where the drag starts to increase significantly due to separated flow. As before, the trim conditions were used to find $C_{D_{\text{trim}}}$ over different flight conditions. Before stall, trim drag values are close to the drag polar fit and after stall, the effects of separated flow increase the drag well above the basic drag polar.

B. Longitudinal Stability

The pitching moment coefficient about the center of gravity versus angle of attack for the SU-26xp was calculated. Figure 4 only shows four different cases of trim angles of attack with each case including a set of flights with approximately the same trim angle of attack. All of the plotted cases have the same center of gravity but different elevator deflections. A least squares fit was used to find the trim angle of attack and C_{M_α} from the pitching moment and angle of attack time history. Figure 4 shows that C_{M_α} increases with angle of attack, and the effect can be further seen when analyzing the neutral point location. The neutral

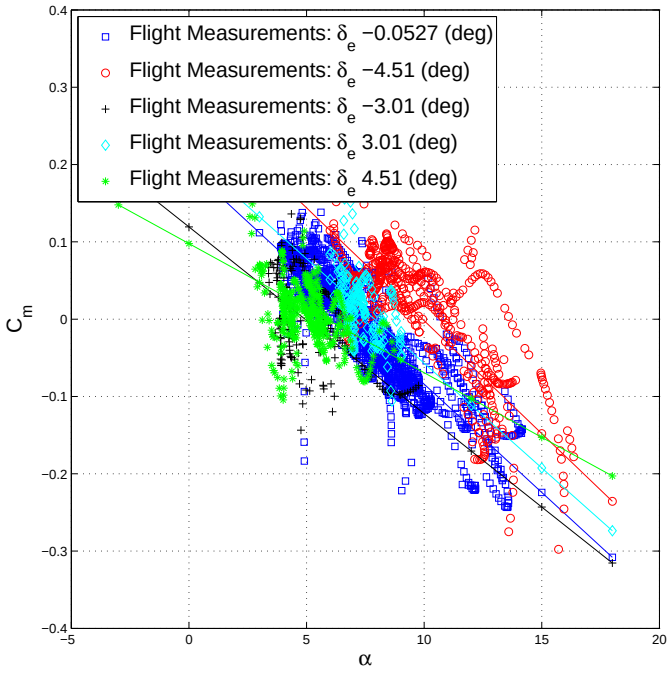

Figure 4. Experimentally measured pitching moment versus angle of attack for the SU-26xp airplane with the center of gravity at 42% of the root chord.

point was found from C_{M_α}, C_{L_α} and the measured location of the center of gravity. Using the experimental lift curve slope (3.61/rad) found earlier, the static margin and experimental neutral point can be found from

$$C_{M_\alpha} = C_{L_\alpha}(SM) \tag{12}$$

where the static margin, SM, is the nondimensional difference between the neutral point and the known center of gravity.

The neutral point is the aerodynamic center of the airplane and is measured from the wing root leading edge in percentage of wing root chord. Theoretical neutral point can be found using[28, 29]

$$l_{np} = \frac{C_{L_{\alpha,\mathrm{w}}}\frac{l_{ac,\mathrm{w}}}{c_\mathrm{w}} + \frac{l_{ac,\mathrm{t}}}{c_\mathrm{w}}C_{L_{\alpha,\mathrm{t}}}\eta_\mathrm{t}\frac{S_\mathrm{t}}{S_\mathrm{w}}(1-\frac{\partial\epsilon}{\partial\alpha})}{C_{L_{\alpha,\mathrm{w}}} + C_{L_{\alpha,\mathrm{t}}}\eta_\mathrm{t}\frac{S_\mathrm{t}}{S_\mathrm{w}}(1-\frac{\partial\epsilon}{\partial\alpha})} \tag{13}$$

where the subscripts of 'w' and 't' represent the values of different variables for wing and horizontal tail respectively. The distance from the aerodynamic center of each surface to a reference point is l_{ac} and it is normalized by the wing root chord, c_w. The surface area of the wing and tail is S_w and S_t, respectively. The downwash and velocity deficit from wake of the main wing at the tail are included in the $\partial\epsilon/\partial\alpha$ and η_t.

As outline in Eq. 13, the neutral point depends on both the lift curve slope of the wing and tail as well as the aerodynamic center of each. The wake from the wing also effects the lift of horizontal tail. In the angle of attack range where both lift curve slopes are linear and the aerodynamic center does not move, the neutral point theoretically stays constant. Using the Eq. 13, the SU-26xp has a theoretical neutral point of approximately 45–49% of the root chord while for the glider it was found to be approximately 41–45% of the root chord.

The experimental neutral point was found using the experimental lift curve slope and the measured center of gravity for each airplane and is shown in Fig 5 for a range of angles of attack. For the SU-26xp, two different CG locations were used with a range of elevator deflections. To analyze the neutral point of the glider, the center of gravity was shifted while glider was in a fixed configuration. The small wing was used and the tail quarter chord was placed 16.0 cm (6.3 in) behind the wing leading edge. While in this configuration, the nose weight was changed to shift the center of gravity, and the tail incidence angle was changed to fly the airplane over a range of angles of attack.

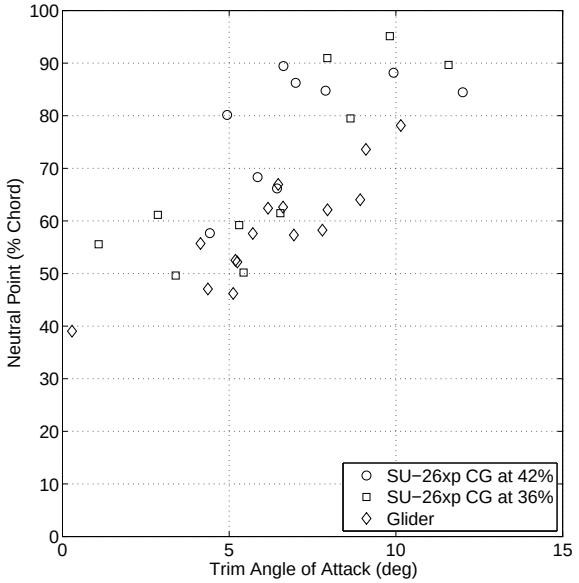

Figure 5. Experimentally measured neutral point (percentage root chord from the wing leading edge) versus trim angle of attack.

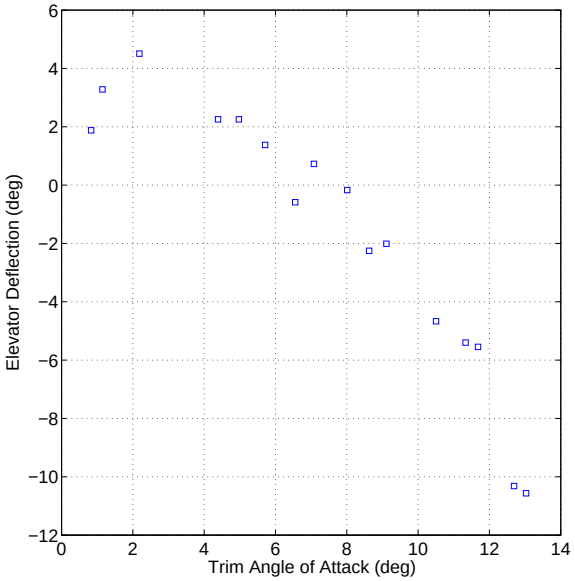

Figure 6. Experimentally measured effect of the elevator deflection on the trim angle of attack for the SU-26xp airplane.

Figure 5 shows the experimentally determined neutral point of the airplanes. For both airplanes, the results show that at low angles of attack, the neutral point is farther forward and close to the previously mentioned theoretical values. As the angle of attack increases, the neutral point moves aft which implies that the tail is becoming more effective with respect to the wing. The shift aft could be caused by a number of different effects changing the performance, particularly the lift curve slope of the wing and/or horizontal tail.

First, the lift curve slope of the main wing (C_{L_α}) decreases gradually at higher angles of attack as shown in Fig. 3 which will cause the neutral point to shift aft. Normally, the tail operates at a lower local angle of attack due to downwash from the main wing. Assuming similar lift curve behavior for the horizontal tail, $C_{L_{\alpha,\mathrm{t}}}$ will also decrease at higher local angles of attack. However, since there is downwash, $C_{L_{\alpha,\mathrm{t}}}$ will decrease at a higher freesteam angle of attack. As the lift curve slope of the main wing decreases with respect to the lift curve slope of the tail, the neutral point of the airplane will move aft.

Second, the induced flow effects from the wake of the main wing on the horizontal tail effects the neutral point. Downwash and the velocity deficit (η_t) caused by the drag of the main wing changes the flow at the horizontal tail. The theoretical formulation includes a $\partial\epsilon/\partial\alpha$ term that assumes the downwash effect is constant with angle of attack. As the flight conditions, particularly α, change the wake of the main wing can move which changes the effect on the horizontal tail. The results indicate that a portion of the downwash and velocity deficit moves above the tail (which is level with the wing for both airplanes) at higher angles of attack. In order to account for this in the theoretical results, both $\partial\epsilon/\partial\alpha$ and η_t must be changed with angle of attack.

Finally, the aerodynamic center of the wing ($l_{ac,\mathrm{w}}$) and tail ($l_{ac,\mathrm{t}}$) probably move aft as the angle of attack increases. At low Reynolds number, the quarter chord pitching moment of the airfoil is normally not constant. In the theoretical calculations, the aerodynamic center of each surface is assumed stay at the quarter chord. However, if the wing and tail aerodynamic centers move aft with increased angle of attack, the shift needs to be included for each surface in the theoretical calculations. While none of these effects can fully explain the neutral point shift, the combination of different effects can explain the shift.

Figure 6 shows the effect of the elevator deflection on the trim angle of attack for the SU-26xp. The SU-26xp elevator was 65% of the horizontal tail area with a deflection range of ± 20 deg, but only a range of 5 to -12 deg was tested to limit the flight regime of the airplane. Increasing positive elevator (trailing edge down) caused the airplane to fly at lower angles of attack. At approximately -3 deg elevator (which is 'up' elevator), the airplane trim angle was 8–9 deg which is the beginning of stall.

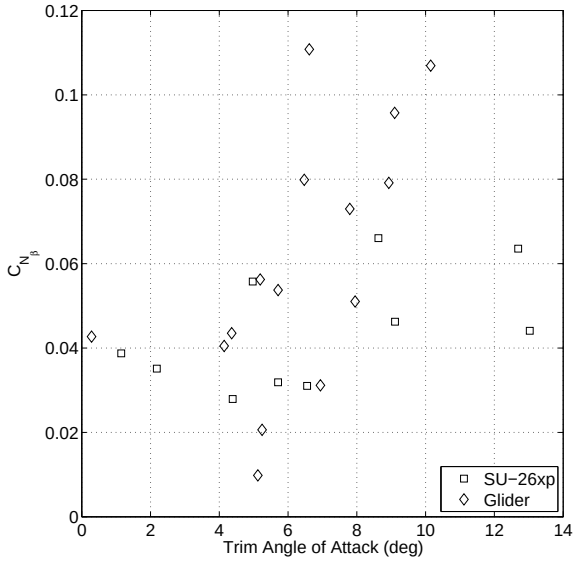

Figure 7. Experimentally measured weathercock stability (C_{N_β}) as a function of trim angle of attack.

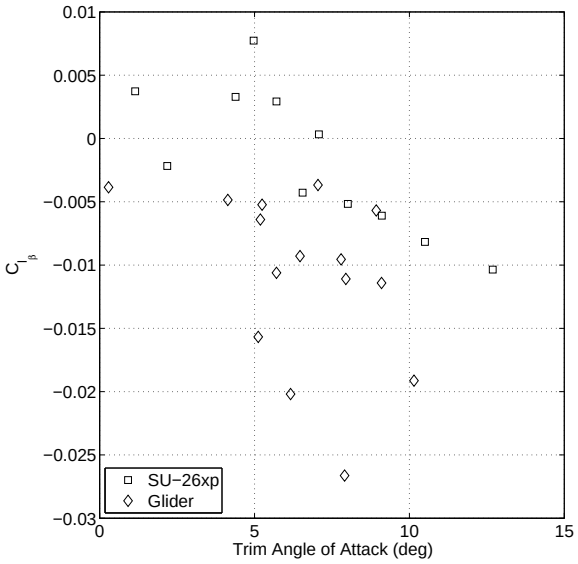

Figure 8. Experimentally measured roll stability (C_{l_β}) as a function of trim angle of attack.

C. Lateral Stability

Static yaw stability of an airplane is ensured by the vertical tail and measured by the yawing moment generated by sideslip angle, C_{N_β}. A positive C_{N_β} ensures the aircraft is stable and any sideslip will damp out. The glider and SU-26xp were stable in yaw over a range of angles of attack as shown by Fig. 7. While there was slight increase in the stability with angle of attack, C_{N_β} stayed within a range of 0.01 to 0.1. In general, the glider had greater weather vane stability than the SU-26xp.

Roll due to yaw, C_{l_β}, is the other major lateral stability derivative for an airplane and is often referred to as the dihedral effect. Negative values of C_{l_β} are stable and along with other lateral stability terms, ensure that when the airplane is perturb it returns to zero sideslip. Figure 8 shows C_{l_β} as a function of angle of attack, and the negative values show that C_{l_β} (along with other terms) contributes to lateral stability for each airplanes. The main wing of the glider has 4.5 deg of dihedral which increases C_{l_β}. For the SU-26xp, which has no dihedral and mid-body wings, the values of C_{l_β} are less than that of the glider. At low angles of attack, a number of C_{l_β} data points (see Fig. 8) for the SU-26xp are positive. As expected, the aerobatic SU-26xp had a lower dihedral effect than the glider.

V. Conclusions

By analyzing the trajectory of the two airplanes, the aerodynamic characteristics of the airplanes were calculated. Experimentally measured lift curve slopes for the low Reynolds number results were smaller than theoretical results as has been observed in other low Reynolds number experimental results. Drag coefficient results showed the induced drag model was an accurate model until separation occurs. At angles of attack greater than stall, the effects of separation cause the drag coefficient to increase above the drag polar.

The longitudinal stability of both the airplanes showed that the neutral point was close to theoretical results at low angles of attack and shifts aft as the angle of attack increases. This shift was probably due to a combination of factors that are changing with angle of attack. These factors include the interactions between the wake of the main wing and the horizontal tail, the lift curve slopes, and the aerodynamic center of each surface. A combination of these factors causes the shift in neutral point observed in the experiments. The glider has higher lateral stability than the aerobatic SU-26xp as expected.

References

[1]Uhlig, D. V., Sareen, A., Sukumar, P., Rao, A. H., and Selig, M. S., "Determining Aerodynamic Characteristics of a Micro Air Vehicle Using Motion Tracking," AIAA Paper 2010–8416, August 2010.

[2]Rhinehart, M. and Mettler, B., "Extracting Aerodynamic Coefficients using Direct Trajectory Sampling," AIAA Paper 2008-6899, 2008.

[3]Mettler, B., "Extracting Micro Air Vehicles Aerodynamic Forces and Coefficients in Free Flight Using Visual Motion Tracking Techniques," *Experiments in Fluids*, February 2010.

[4]Selig, M. S., Guglielmo, J. J., Broeren, A. P., and Giguère, P., *Summary of Low-Speed Airfoil Data, Vol. 1*, SoarTech Publications, Virginia Beach, Virginia, 1995.

[5]Selig, M. S., Lyon, C. A., Giguère, P., Ninham, C. N., and Guglielmo, J. J., *Summary of Low-Speed Airfoil Data, Vol. 2*, SoarTech Publications, Virginia Beach, Virginia, 1996.

[6]Lyon, C. A., Broeren, A. P., Giguère, P., Gopalarathnam, A., and Selig, M. S., *Summary of Low-Speed Airfoil Data, Vol. 3*, SoarTech Publications, Virginia Beach, Virginia, 1998.

[7]Selig, M. and McGranahan, B., *Wind Tunnel Aerodynamic Tests of Six Airfoils for Use on Small Wind Turbines*, National Renewable Energy Laboratory/SR-500-34515, October 2004.

[8]Laitone, E. V., "Wind Tunnel Tests of Wings at Reynolds Numbers below 70,000," *Experiments in Fluids*, Vol. 23, 1997.

[9]Pelletier, A. and Mueller, T. J., "Low Reynolds Number Aerodynamics of Low-Aspect-Ratio, Thin/Flat/Cambered-Plate Wings," *Journal of Aircraft*, Vol. 37, No. 5, September 2000, pp. 825–832.

[10]Mueller, T. J. and Torres, G. E., "Low-Aspect-Ratio Wing Aerodynamics at Low Reynolds Numbers," *AIAA Journal*, Vol. 42, No. 5, May 2004, pp. 865–873.

[11]Spedding, G. R. and McArthur, J., "Span Efficiencies of Wings at Low Reynolds Numbers," *Journal of Aircraft*, Vol. 47, No. 1, January 2010, pp. 120–128.

[12]Torres, G. E. and Mueller, T. J., "Aerodynamics of Low Aspect Ratio Wings at Low Reynolds Numbers with Applications to Micro Air Vehicle Design and Optimization," Tech. Rep. 20011221 033, Naval Research Lab, November 2001.

[13]Klein, V. and Morelli, E. A., *Aircraft System Identification: Theory and Practice*, AIAA Education Series, AIAA, Reston, VA, 2006.

[14]Jategaonkar, R. V., *Flight Vehicle System Identification: A Time Domain Methodology*, AIAA Progress in Astronautics and Aeronautics, AIAA, Reston, VA, 2006.

[15]Johnson, E. N., Turbe, M. A., Wu, A. D., Kannan, S. K., and Neidhoefer, J. C., "Flight Test Results of Autonomous Fixed-Wing UAV Transitions to and from Stationary Hover," AIAA Paper 2006-6775, 2006.

[16]Vicon MX System, *System Reference: Revision 1.7*, Vicon Motion Systems, Oxford, UK, 2007.

[17]Hoburg, W. and Tedrake, R., "System Identification of Post Stall Aerodynamics for UAV Perching," AIAA Paper 2009-1930, 2009.

[18]Cory, R. and Tedrake, R., "Experiments in Fixed-Wing UAV Perching," AIAA Paper 2008-7256, 2008.

[19]Blauwe, H. D., Bayraktar, S., Feron, E., and Lokumcu, F., "Flight Modeling and Experimental Autonomous Hover Control of a Fixed Wing Mini-UAV at High Angle of Attack," AIAA Paper 2007-6818, 2007.

[20]Frank, A., McGrew, J. S., Valentiz, M., Levinex, D., and How, J. P., "Hover, Transition, and Level Flight Control Design for a Single-Propeller Indoor Airplane," AIAA Paper 2007-6318, 2007.

[21]Sobolic, F. M. and How, J. P., "Nonlinear Agile Control Test Bed for a Fixed-Wing Aircraft in a Constrained Environment," AIAA Paper 2009-1927, 2009.

[22]How, J. P., "Multi-Vehicle Flight Experiments: Recent Results and Future Directions," *Proceedings of the Symposium on Platform Innovations and System Integration for Unmanned Air, Land and Sea Vehicles*, Neuilly-sur-Seine, France, 2007.

[23]Paley, D. A. and Warshawsky, D. S., "Reduced-Order Dynamic Modeling and Stabilizing Control of a Micro-Helicopter," AIAA Paper 2009-1350, 2009.

[24]Ducard, G. and D'Andrea, R., "Autonomous Quadrotor Flight Using a Vision System and Accommodating Frames Misalignment," *IEEE International Symposium on Industrial Embedded Systems*, Lausanne, Switzerland, 2009.

[25]E-Flite, "Sukhoi SU-26xp," http://www.e-fliterc.com/Products/Default.aspx?ProdID=PKZU1080, Accessed November 2010.

[26]MATLAB, *Curve Fitting Toolbox™ 2 Users Guide*, The Mathworks Inc, Natick, MA, March 2010.

[27]Stevens, B. L. and Lewis, F. L., *Aircraft Control and Simulation*, Wiley-Interscience, New York, NY, 1st ed., 1992.

[28]McCormick, B. W., *Aerodynamics Aeronautics and Flight Mechanics*, John Wiley & Sons, New York, 2nd ed., 1995.

[29]Phillips, W., *Mechanics of Flight*, John Wiley and Sons, Inc, New Jersey, 1st ed., 2004.